Journal of
Materials Chemistry B

Materials for biology and medicine

Accepted Manuscript

ROYAL SOCIETY OF CHEMISTRY

rsc.li/materials-b

Halogen-free photosensitizers based on meso-enamine-BODIPYs for bioimaging and photodynamic therapy

Ruth Prieto-Montero,[1†] Aitor Díaz Andres,[2†] Alejandro Prieto-Castañeda,[3†] Andrea Tabero,[4] Asier Longarte,[5] Antonia R. Agarrabeitia,[3,6] Angeles Villanueva,[4] María J. Ortiz,[3] Raúl Montero,[7*] David Casanova[2,8*] and Virginia Martínez-Martínez[1*]

[1]Departamento de Química Física, Facultad de Ciencia y Tecnología, Universidad del País Vasco/Euskal Herriko Unibertsitatea (UPV/EHU), 48080 Bilbao, Spain.

[2]Donostia International Physics Center (DIPC), 20018 Donostia, Euskadi, Spain.

[3]Departamento de Química Orgánica, Facultad de CC. Químicas, Universidad Complutense de Madrid, 28040 Madrid, Spain.

[4]Departamento de Biología, Universidad Autónoma de Madrid, Darwin 2, 28049 Madrid, Spain.

[5]Spectroscopy Laboratory, Departamento Química Física, Facultad de Ciencia y Tecnología, Universidad del País Vasco/Euskal Herriko Unibertsitatea (UPV/EHU), Apartado 644, 48080 Bilbao, Spain.

[6]Sección Departamental de Química Orgánica, Facultad de Óptica y Optometría, Universidad Complutense de Madrid, Arcos de Jalón 118, 28037 Madrid, Spain.

[7]SGiker Laser Facility, Universidad del País Vasco (UPV/EHU), Sarriena s/n, 48940 Leioa, Spain.

[8]IKERBASQUE, Basque Foundation for Science, 48009 Bilbao, Euskadi, Spain.

* Correspondence: virginia.martinez@ehu.eus; Tel.: +34-946-015-969

† Equal contribution

Abstract

The search for efficient heavy atom free photosensitizers (PS) for photodynamic therapy (PDT) is a very active field. We describe herein a simple and easily accessible molecular design based on the attachment of an enamine group as an electron-donor moiety at the *meso* position of the BODIPY core with different alkylation patterns. The effect of the alkylation degree and solvent polarity on the photophysical properties in terms of splitting absorption bands, fluorescence efficiencies and singlet oxygen production is deeply analyzed experimentally by spectroscopic techniques, including femtosecond and nanosecond transient absorption (fs- and ns-TA) and by computational simulations based on time-dependent density functional theory. The correlation between the theoretical/experimental results permits to rationalize the observed photophysical behavior exhibited by the *meso*-enamine-BODIPY compounds and to determine the mechanistic details, which rule the population of the triplet state manifold. The potential applicability as

theragnostic agents for the most promising compound is demonstrated through *in vitro* assays in HeLa cells analyzing the internalization, localization and phototoxic action.

Keywords

Halogen-free BODIPY photosensitizer, enamine-donor group, charge transfer state, singlet oxygen, theoretical simulations, *in vitro* HeLa assays

Introduction

The search for single systems able to diagnose and treat diseases, mainly cancer, has attracted great interest in modern medicine. Theragnosis (diagnosis and therapy) permits the *in situ* visualization of cancer tissues and cells, enhancing its treatment.[1–4] Nevertheless, obtaining a theragnostic agent is not a trivial task.[5–9] A promising route could be the combination of fluorescent bioimaging for diagnosis and photodynamic therapy (PDT) as treatment, by the use of organic dyes.[4,10–16] PDT requires the presence of molecular oxygen (O_2), the organic dye (photosensitizer) and a specific light source. In PDT, the photosensitizer (PS) is activated under light, generating reactive oxygen species (ROS), mainly singlet oxygen ($^1O_2$), Figure 1. This species of oxygen are cytotoxic and able to destroy cancer cells by apoptosis or necrosis.[17–19] However, fluorescence and ROS generation are competing photophysical processes and a suitable balance between these antagonistic features should be pursued.[20–23]

Recently, one type of new lab-made PSs are based on the BODIPY chromophore (boron dipyrromethene), considered a chemically versatile small chromophore with excellent photophysical properties (intense absorption and emission bands and high photoresistance), stable under physiological conditions and insensitive to environmental changes.[24–27] One strategy to design a theragnostic agent is the reduction of fluorescence by adding heavy atoms such as transition metals (Ru, Pd or Pt) or halogen atoms (Br or I) into the fluorophore structure, enhancing the intersystem crossing (ISC) driven by spin-orbit coupling (SOC) and as a consequence, increasing the triplet state population,[19,20,22,28–32] Figure 1A. For instance, by the addition of heavy atoms to the BODIPY core, especially iodinated atoms at 2 and 6 positions, its fluorescence drastically decreases in favor of the triplet state population by ISC ($S_1 \rightarrow T_n$), and high singlet oxygen generation is achieved.[18,20,24,31,33–39] Nevertheless, the efficiency of the photosensitizing action depends significantly on the lifetime of the lowest triplet state (T_1) and the presence of the heavy atom increases also the ISC process back to the ground state ($T_1 \rightarrow S_0$), considerably reducing the triplet state lifetime. Besides, halo-BODIPYs suffer from poor photostability and undesirable toxicity, diminishing their applicability and biocompatibility for biomedical uses.[18,19,37]

To address these drawbacks, the design of heavy atom-free photosensitizers is currently a very active research field.[40–53] One of the strategies relies on the combination of electron donor (D) and acceptor (A) moieties to induce charge transfer (CT) states, which can act as mediators between

singlet and triplet excited states by two different pathways: radical pair intersystem crossing (RP-ISC)[54,55] or spin-orbit charge transfer intersystem crossing (SOCT-ISC),[56–59] Figure 1B. Roughly, RP-ISC usually occurs when the electronic coupling between D and A units is weak, *e.g.*, in spatially separated dyads by a linker, whereas the SOCT-ISC efficiency rapidly decays with the distance and it often takes place in directly linked D-A structures with a nearly orthogonal disposition. Generally, by these types of mechanisms, singlet oxygen generation (triplet population) and fluorescence efficiency (singlet population) of PSs can be efficiently modulated by the relative electron ability of A and D units, their chemical connection and relative geometrical disposition, as well as the polarity of the media.[8,46,47,57,60–63]

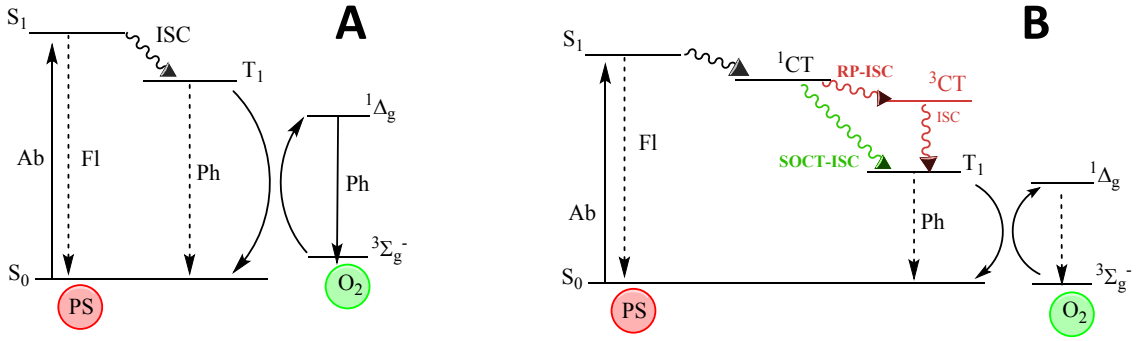

Figure 1. Jablonski diagram showing population of triplet states by conventional intersystem crossing (ISC) mechanism from the first singlet excited state (A) and by radical-pair intersystem crossing (RP-ISC) or by spin-orbit charge transfer intersystem crossing (SOCT-ISC) mechanisms (B).

Some examples of halogen-free BODIPYs, in which different electron-donor groups have been incorporated into the chromophore core,[39,45,47,48,53,63–67] have been already reported as potential theragnostic agents. In most cases, the electron-donating unit is added to the *meso* position, considered the most sensitive one in terms of photophysics impact because of the marked change of the electronic density that undergoes upon excitation (Figure 2-Top).

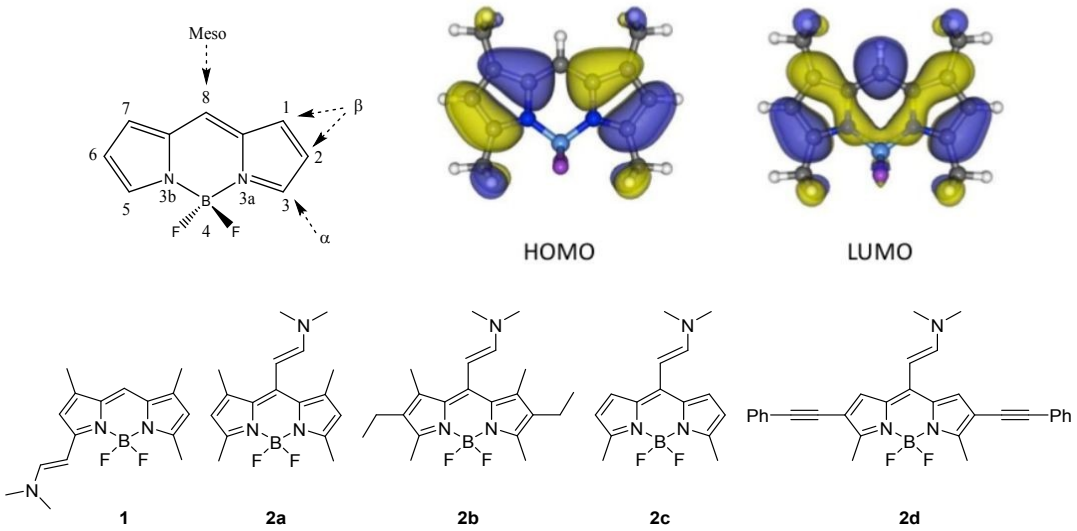

Figure 2. Top) General BODIPY structure. The different positions in the core are indicated and numbered according to the IUPAC system.[68] Frontier orbitals involved in the lowest electronic transitions (HOMO and LUMO) of a representative BODIPY; Bottom) Molecular structures of the different enamine substituted BODIPY derivatives.

In this work, unlike other previous studies, a small group, of enamines, is selected as electron donor substituent in the set of studied BODIPYs showed in Figure 2.[39,45,48,53,63,65–67,69] All these compounds were synthesized by Vilsmeier-Haack reaction, showing a new family of structurally simple and easily accessible compounds with push-pull character.[70] Firstly, the effect exerted on the photophysics by the substitution of this group at *α- vs meso*-positions of the BODIPY core is compared (**1** *vs* **2a** in Figure 2-Bottom). Then, in the search for the best fluorescent-PS agent for PDT, several *meso*-enamine-BODIPY derivatives varying the alkylation pattern of the BODIPY core are analyzed (**2a-2c**, Figure 2-Bottom). The effects of the alkylation degree and solvent polarity on the resultant photophysical features are deeply analyzed by theoretical simulations that allow characterizing the electronic states involved in the excitation/relaxation processes. To further understand the observed photophysical behavior, the relaxation pathway and the energy of the involved states were explored by femtosecond and nanosecond transient absorption (TA) and triplet energy and lifetime characterization. Finally, the collected evidences allow us to postulate a new BODIPY, with ethynyl phenyl groups at 2- and 6-positions to extend the delocalization of the π-system (**2d** in Figure 2), as a suitable candidate with a red-shifted absorption band for theragnostic applications. The internalization, localization and phototoxic action of this compound are tested *in vitro* in HeLa cells with very promising results.

Results and Discussion

Enamine substitution of BODIPY

Firstly, the impact of the position of the donor enamine group on the photophysical properties was analyzed by comparing the enamine-BODIPYs substituted at 3- or *meso*-position (**1** *vs* **2a**). As expected, the enamine substitution at *α*-position extends the π-conjugation of the BODIPY core, as shown by the π-electron distribution of the highest occupied (HOMO) and the lowest unoccupied (LUMO) molecular orbitals (Figure S1), which induces a bathochromic shift with respect to the unsubstituted green BODIPYs, placing their respective absorption and emission bands in the orange region of the visible spectra (575 nm and 593 nm, respectively, Table 1). The relative shift in the absorption bands of **1** and **2a** is well recovered by the computed vertical excitations at the Franck-Condon region (Table S1). Compound **1** keeps a relatively high fluorescence quantum yield (60%) and negligible singlet oxygen production (Figure 3 and Table 1).

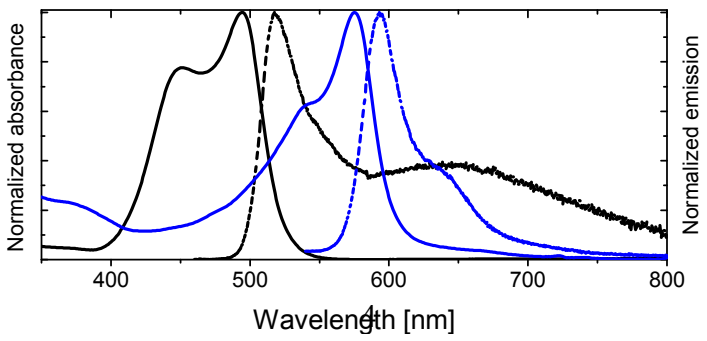

Figure 3. Height-normalized absorption (solid curves) and emission spectra (dash curves) in chloroform for **1** (blue) *vs* **2a** (black).

Conversely, by simply attaching the enamine group at *meso* position, the photophysical properties of the BODIPY are drastically changed. Compound **2a** brings an important difference in the location of their respective spectroscopic bands, shifted to shorter wavelengths with respect to compound **1** (Table 1 and Figure 3). This hypsochromic effect is typically found when electron donor groups are anchored in *meso* position, especially for amine groups.[71,72] Moreover, the absorption spectra, unlike common BODIPY dyes, show an important shoulder contribution at shorter wavelengths, placed at around 450 nm. The formation of H-type aggregates is discarded as the spectrum is registered at diluted solution (~ 2 x 10^{-6} M). The nature of this contribution will be discussed in detail below. Besides, the enamine substitution at *meso* position induces a drastic fluorescence emission quenching, shortening their lifetimes (Table 1). Although the fluorescence is weak for **2a** (Table 1), it was possible to record a dual emission (Figure 3, Table 1), showing a narrower emission band at 518 nm assigned to the locally excited (LE) state and a broader band centered at around 640 nm, characteristic of a radiative deactivation of an intramolecular charge transfer state (CT).[73,74] Although the presence of the enamine unit at *meso* position in compound **2a** enhances non-radiative deactivation pathways, the triplet state is not effectively populated, yielding a relative low singlet oxygen production (4% in chloroform, Table 1).

Role of alkylation on *meso*-enamine substituted BODIPYs

Further alkylation of the BODIPY core with two extra ethyl groups at 2,6-positions, compound **2b**, does not ameliorate the photophysical properties (Table 1), rendering practically null fluorescence and singlet oxygen production in all solvents of any polarity (Table 1 and Table S3). Intriguingly, the absorption spectrum of compound **2b** clearly shows two independent bands, with the peak centered at shorter wavelengths slightly blue-shifted with respect to the previously denoted as a shoulder for compound **2a**. Contrarily, the main absorption band is red-shifted with respect to that recorded for the homologous compound **2a** (Table 1 and Figure 4A). The splitting of the two absorption bands of **2b** increases as the polarity of the solvent decreases (Figure 4B). Decreasing the polarity of the solvent, acetonitrile > chloroform > toluene > c-hexane, has a double effect on the absorption peak at shorter wavelengths, that is, a gradual intensity decrease and a hypsochromic shift. On the other hand, the main absorption band (at higher wavelengths) suffers a bathochromic shift and becomes progressively more intense. Indeed, for apolar solvents, *e.g.,* c-hexane, the absorption bands are nicely divided into two distinguished peaks. On the contrary, in polar solvents, *e.g.*, acetonitrile, both absorption contributions overlap as they become closer in energy and intensity.

Table 1. Photophysical properties and singlet oxygen quantum yield in chloroform for enamine-BODIPY compounds; absorption maxima (λ_{ab}), molar absorption coefficient (ε_{max}), fluorescence maxima (λ_{fl}), fluorescence quantum yield (Φ_{fl}), fluorescence lifetime (τ_{fl}) and singlet oxygen quantum yield (Φ_{Δ}).

Compound	λ_{ab} (nm)	ε_{max} 10^{-4} ($M^{-1}cm^{-1}$)	λ_{fl} (nm)	Φ_{fl}	τ_{fl}^{*} (ns)	Φ_{Δ}

1	575	4.3	593	0.60	0.69 (10%) 4.04 (90%)	0
2a	494/451	5.7	518/640	<0.01	-	0.04
2b	516/449	3.3	540/670	<0.01	-	0
2c	496/460	6.6	529	0.08	0.92 (97%) 5.29 (3.0%)	0.20
2d	551/490	5.7	599	0.42	3.23	0.31

* λ_{ex} = 530 nm, λ_{em} = 585 nm (for **1**); λ_{ex} = 480 nm, λ_{em} = 530 nm (for **2c**); λ_{ex} = 490 nm, λ_{em} = 600 nm (for **2d**).

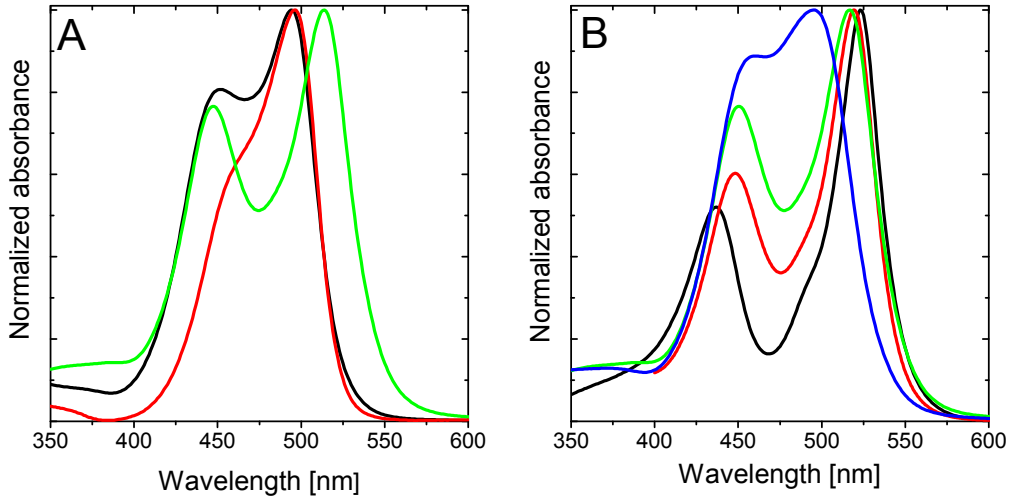

Figure 4. (A) Normalized absorption spectra of **2a** (black), **2b** (green) and **2c** (red) in chloroform; and (B) normalized absorption spectra for **2b** in different solvents: c-hexane (black), toluene (red), chloroform (green) and acetonitrile (blue).

To get insight on the nature of the two bands in the absorption spectra, rationalize the differences between the studied compounds and understand the changes induced by the polarity of the solvent, we have carried out electronic structure calculations for molecules **2a-c**. The ground state energy minimum of molecule **2b** exhibits a relative torsion of θ ~ 30º between the group in the *meso* position and the BODIPY's molecular plane. Nonplanarity is promoted by steric hindrance of the enamine with the methyl groups in positions 1 and 7. TDDFT calculations at the Franck-Condon geometry identify the two lowest singlet-to-singlet electronic transitions in **2b** as optically active, *i.e.*, with large oscillator strengths, in good agreement with the presence of two absorption bands registered in solution (Figure 4). The lowest excited singlet state is mainly obtained as the excitation from the HOMO to the LUMO, whereas S_2 can be described as the electronic promotion from the HOMO-1 to the LUMO (Figure 5a). The HOMO of **2b** is localized on the BODIPY unit, while the HOMO-1 emerges from the coupling of the enamine and BODIPY π-systems. Finally, the LUMO is largely delocalized over both enamine and BODIPY moieties.

Interestingly, frontier orbital energies change with the polarity of the environment. Concretely, solvents with larger dielectric constants stabilize and destabilize the HOMO and HOMO-1, respectively (Figures 5b and 5c). On the other hand, the energy of the LUMO remains rather constant. As a consequence, the transition energy to S_1 (S_2) increases (decreases) with the

solvent's polarity, and the S_1 to S_2 energy gap decreases. It is worth noticing that the computed oscillator strengths (*f*) suggest a change in the relative intensity of the two bands, with $f(S_2)/f(S_1)$ ratio increasing with the polarity of the solvent (Table 2). These results explain the change in the absorption profiles upon the change in the solvent polarity, *i.e.,* frequency shift of the two bands and the change in relative intensities (Figure 4B).

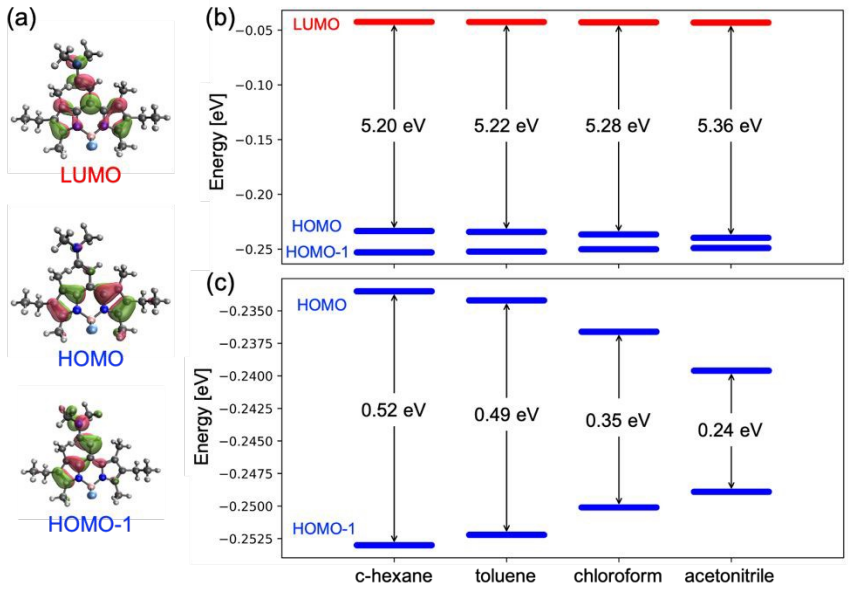

Figure 5. (a) Frontier molecular orbitals of **2b** computed with CAM-B3LYP/cc-pVDZ in chloroform. (b) Orbital energy diagram (in eV) of **2b** in c-hexane, toluene, chloroform and acetonitrile. (c) Zoom of HOMO and HOMO-1 orbital energies.

Table 2. Vertical excitation energies (in eV) to S_1 and S_2 for compound **2b** computed at the CAM-B3LYP/cc-pVDZ level in different solvents: c-hexane, toluene, chloroform, and acetonitrile. Oscillator strength of the transitions indicated in parenthesis. ΔE (in eV) is the S_1 to S_2 energy separation.

Solvent	$E(S_1)$	$E(S_2)$	ΔE
c-hexane	2.86 (0.635)	3.32 (0.588)	0.46
toluene	2.88 (0.628)	3.30 (0.599)	0.42
chloroform	2.90 (0.624)	3.22 (0.651)	0.32
acetonitrile	2.98 (0.569)	3.21 (0.649)	0.23

Dealkylation of positions 2 and 6 in **2a** with respect to **2b** preserves the torsion of the enamine with respect to the BODIPY fragment. The main difference between the electronic structure of **2a** and **2b** is the orbital energy of the HOMO, since it is the frontier orbital presenting the largest electron density at the 2 and 6 carbon atoms. Substitution of the alkyl groups by a more electronegative hydrogen stabilizes the HOMO (Figure S2), shifting the S_1 transition to shorter wavelengths and reducing the energy separation between S_1 and S_2 states (Table 3), in agreement with the absorption spectra (Figure 4A). Similarly, dealkylation of positions 1 and 7 in **2c** mainly stabilizes the HOMO and LUMO, as both orbitals present sizeable electron densities on these atoms. As a consequence, the S_1 energy barely changes with respect to **2a**, while the S_2 transition slightly redshifts (~0.1 eV), resulting in a rather small separation between S_1 and S_2 transitions.

In fact, the absorption spectrum of **2c** does not show a noticeable shoulder feature at shorter wavelengths and the main band resembles to the one for pristine BODIPY (no substitution). It is worth noticing that the no-alkylation in 1 and 7 atoms slightly increases the molecular planarity in **2c** ($\theta \sim 26^{o}$) with respect to **2b** and **2a**, allowing for a larger electronic mixing of the BODIPY and enamine π-systems (Figure S1).

Table 3. Vertical excitation energies (in eV) to S_1 and S_2 for compounds **2a**, **2b** and **2c** computed at the CAM-B3LYP/cc-pVDZ level in chloroform. Oscillator strength of the transitions indicated in parenthesis. ΔE (in eV) is the S_1 to S_2 energy separation.

Molecule	$E(S_1)$	$E(S_2)$	ΔE
2b	2.90 (0.624)	3.22 (0.651)	0.32
2a	3.00 (0.585)	3.25 (0.635)	0.25
2c	3.02 (0.559)	3.12 (0.692)	0.10

On the other hand, regarding the fluorescence and singlet oxygen quantum yield, our results clearly indicate that methylation at 1- and 7- in *meso*-enamine-BODIPYs noticeably influences the fluorescence efficiency, and more significantly, the singlet oxygen generation (Tables 1 and S3). Compound **2c**, without methyl groups at 1- and 7- positions, shows the highest singlet oxygen and fluorescence quantum yields of the series, whereas compounds **2a** and **2b** show nearly no emission and singlet oxygen production, being internal conversion (IC) the main deactivation pathway (see next section). Moreover, the fluorescence quantum yield and also the singlet oxygen quantum yield of **2c** increase as the polarity of the solvent decreases (Table S3). The less efficient radiative deactivation of the singlet excited state, as well as the singlet to triplet transition in polar solvents, was also observed for other BODIPYs dyads.[47,57,60]

Decay dynamics of photoactivated enamine-BODIPYs

In order to extract mechanistic information on the excited state relaxation of the present compounds, TA experiments have been carried out on **2b** (Figure 6) and **2c** (Figure 7), considered as representative examples in terms of methylation degree, in solvents with different polarities (toluene, $CHCl_3$ and ACN). Figure 6a shows the TA spectra of **2b** in toluene at selected pump-probe delays. At short delays (0.15 ps) the TA spectrum is composed mainly by 3 contributions: a positive band at 350-400 nm attributable to excited state absorption (ESA), the ground state bleach (GSB) at 425-525 nm and a lower negative feature extending from 525 to 700 nm and corresponding to stimulated emission (SE). The blue end of the latter contribution reflects the emission from the initially prepared excited state. It decays in 1 ps, denoting a short living LE state. Within the same time scale, a positive feature appears at 570 nm corresponding to the absorption from an excited species formed during the LE state decay. The comparison with previous studies on BODIPY donor and acceptor groups[75] allows us to identify this feature as the absorption of a CT state, in which the enamine plays the role of the donor and the BODIPY core acts as the acceptor. The remarkable red shift of the emission during the first picoseconds seems to support this hypothesis.

A multiexponential fit with four components (τ_1 = 1.1 ps; τ_2 = 19 ps; τ_3 = 118 ps; τ_4 > 5 ns) yields a satisfactory description of the transient spectra. The distribution of preexponential factors

resulting from this analysis is presented in the decay associated spectra (DAS) in Figure 6b (See supporting information section for further details on the data analysis). As it is observed there, for **2b** the amplitude of the slower decay (a_4) is negligible, but it is included for later comparison with **2c**. The distribution of a_1 (τ_1 = 1.1 ps) shows changes in the ESA band without affecting the evolution of the GSB, meaning that the nature of the excited state is modified in this time scale. Indeed, a_1 describes simultaneously the LE emission decay (550 nm) and the onset of the CT features (positive band at 570 nm and emission at wavelengths > 650 nm). Therefore, a_1 accounts for the population that being initially excited to S_1 (LE), reaches the CT state. Regarding τ_3, as displayed by the GSB band, the excited state population decays to the ground state with this 118 ps lifetime. The spectral characteristics of the CT state in the 500-700 nm region are also perceptible in the a_3 distribution, which indicates that IC to the ground state mainly occurs from the CT state. Finally, the scrutiny of a_2 reflects that certain CT formation takes place in a slower time scale (τ_2 = 19 ps). In fact, a_1 and a_2 spectra are very similar except for the emission contribution in the red edge. Differently, a_2 shows emission at intermediate wavelengths between the LE and CT bands, which could be related to the cooling (vibrational relaxation) on the CT potential well.

A higher polarity solvent as $CHCl_3$ (panels c and d in Figure 6) does not change qualitatively the dynamics, as illustrated by the resemblance of the transient spectra and DAS with those in the previous solvent. Only a substantial acceleration of the CT formation is noticeable. Thus, in $CHCl_3$, τ_1 and τ_2 are respectively 0.6 and 3.5 ps, while IC remains almost unaltered (τ_3 = 112 ps). Following the same trend, Figures 6e and 6f show that further stabilization of the CT state with a higher-polarity solvent (ACN) gives rise to even faster dynamics (τ_1 = 0.2 ps; τ_2 = 1.3 ps; τ_3 = 13 ps; τ_4 = 78 ps). In this case, two components of tens of picoseconds, τ_3 and τ_4, account for the independent radiativeless relaxation pathways of the CT state. The origin of this dual deactivation channels to the ground state is unclear.

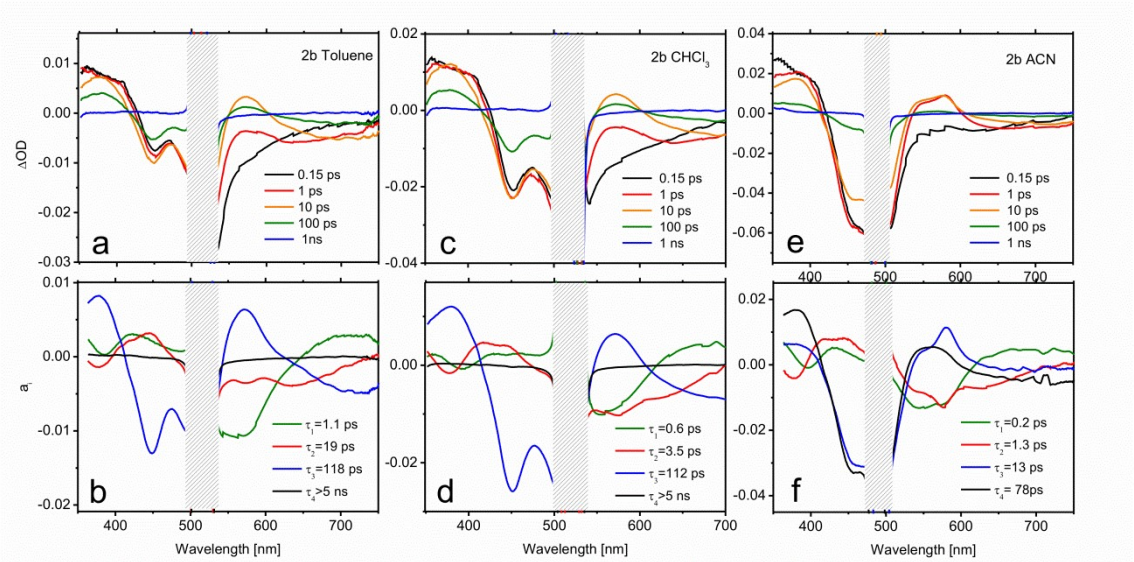

Figure 6. Transient spectra and DAS of **2b** in toluene (a, b), $CHCl_3$ (c, d) and ACN (e, f).

Although notable differences in the kinetics are observed for **2c**, its TA data (Figure 7) can be understood by the same basic model than that employed for **2b.** In toluene, the decay of the LE

fluorescence and the onset of the red shifted emission of the CT formation take place in τ_1 = 1.7 ps and τ_2 = 28 ps, respectively (Figure 7b). The decay of the CT state described by the a_3 spectrum is much slower in this case (τ_3 = 1.8 ns). It is also worth noting that the CT emission in **2c** covers the 520-600 nm region, pointing to a less marked CT character. Indeed, the CT absorption band at 570 nm appears now as a small dip on top of the emission band. The most remarkable feature in the relaxation of **2c** is the appearance of a very long-living species (τ_4 > 5 ns) that can be identified as the T_1 state on the basis of its TA spectrum (a_4). This triplet state has to be formed from the CT relaxation, although its formation dynamics cannot be resolved from the recorded data. The triplet quantum yield can be determined on the grounds of a_4 component through the ratio between the GSB band maximum in the a_4 spectrum and at t = 0 ns, yielding a value of Φ_T = 0.37. This number is in total agreement with the singlet oxygen quantum yield obtained in this solvent by the direct registration of its photoluminescence signal (Table S3). Moreover, the assignation of TA spectrum at τ_4 > 5 ns to the triplet state absorption features is confirmed by the registration of the TA spectra in the nanosecond range (Figure S3). Similarly, the ns-resolved TA (ns-TA) presents a positive band around 375-430 nm, attributed to the absorption of the T_1 state, a negative contribution in the 425-525 nm that corresponds to the ground state bleaching (GSB) associated with the $S_0 \rightarrow S_1$ transition, and a weak and broad contribution at > 525 nm, also assigned to triplet absorption.[47,60,74,76,77] The lifetimes registered at 405 nm and 540 nm measured under nitrogen-saturated conditions were 16 µs, long enough for an efficient quenching by oxygen (Figure S3). The spin-triplet multiplicity nature of this state is confirmed by the quenching registered within the triplet lifetime range under aerated conditions (Table S4).

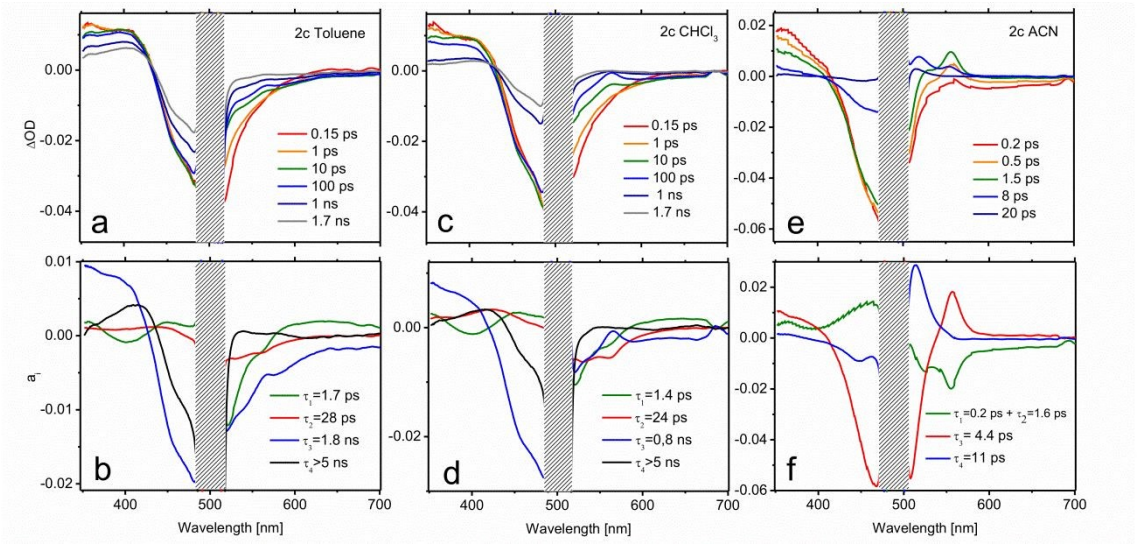

Figure 7. Transient spectra and DAS of **2c** in toluene (a, b), $CHCl_3$ (c, d) and ACN (e, f).

The CT dynamics of **2c** in $CHCl_3$ is very similar. However, its lifetime is noticeably shorter (τ_3 = 0.8 ns) and the triplet quantum yield is lower (Φ_T = 0.24), which is once again in agreement with the singlet oxygen production obtained in this solvent. This fact suggests that the formation of a long-lived CT state is required in order to efficiently couple to the triplet state. The ns-TA spectrum is comparable to that obtained in toluene (Figure S3), but a much longer triplet lifetime is registered (113 µs, Table S4). Finally, in ACN, an extremely fast relaxation of the CT is observed (panels e and f in Figure 7 and Figure S5). The formation of the CT state occurs at a

similar scale (τ_1 = 0.2 ps and τ_2 = 1.6 ps), which, owing to their very similar spectra, have been plotted together in Figure 7f for simplicity. However, the subsequent decay is much faster, draining the population to the ground state with τ_3 = 4.4 ps. This channel precludes the formation of the triplet state. Accordingly, the distribution of a_4 is compatible with the cooling of the excitation energy in the ground state (vibrational relaxation) that is now perceptible due to the very fast IC.

Further experiments were also carried out for **2b** and **2c** in $CHCl_3$ using excitation energies resonant with the S_2 state (445 nm). The observed dynamics was essentially the same recorded after pumping to S_1, pointing to a very fast S_2-S_1 conversion in both species (Figure S6).

ISC mechanism

TA measurements for **2b** and **2c** indicate that triplet state population occurs from a CT state, suggesting a SOCT mechanism. Electronic structure calculations for **2c** identify two excited state minima on the S_1 potential energy surface. At small torsion angles between BODIPY and the *meso*-enamine fragments, there is a local S_1 minimum with the hole and electron largely localized on the BODIPY and with participation of the enamine's π-system, which can be related to the LE state identified by TA spectroscopy (Figure 8). The LE geometry exhibits a small enamine-BODIPY dihedral angle (~20°) and presents a sizeable transition dipole moment and oscillation strength to the ground state (Table S2). Hence, we identify it as the state responsible for the fluorescence emission recorded in the 500-540 nm region. Additionally, the molecule presents a lower energy excited state minimum with an orthogonal disposition between the two fragments in which the hole is localized on the enamine unit and the electron on the BODIPY fragment, *i.e.,* a CT state. Notably, the relative energy between LE and CT states strongly depends on the solvent's polarity, with polar solvents stabilizing the orthogonal CT with respect to the LE state. The vertical energy gap to the ground state at the CT minimum severely diminishes with increasing the polarity of the solvent (Table S2), in line with the increase of non-radiative decay rates and the hindering of singlet oxygen generation.

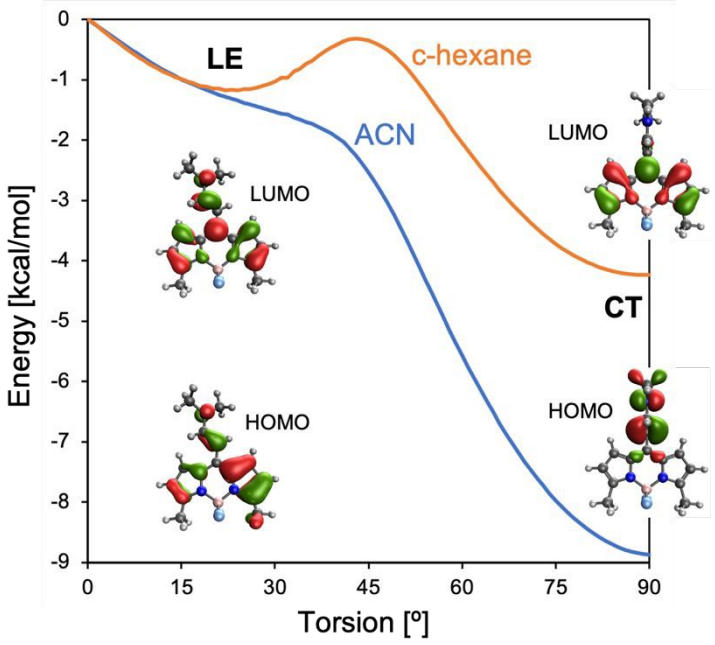

Figure 8. Energy profiles (in kcal/mol) of the lowest excited singlet state (S_1) of **2c** computed in c-hexane (orange) and ACN (blue) along the molecular torsion between BODIPY and enamine moieties. Molecular torsion model has been obtained by constrained geometry optimization of S_1 state in ACN at different torsion angles. S_1 energies relative to the value at the planar arrangement. Inset: HOMO and LUMO for the LE and CT states.

At the LE minimum, although the S_1 state presents non-vanishing SOCs to the two lowest triplet states, singlet-triplet energy gaps are rather large, preventing for efficient ISC, as in pristine BODIPY (Figure 9). On the other hand, molecular torsion towards the CT minimum largely reduces S_1/T_n energy differences and modifies the electronic nature of low-lying states. Along the molecular orthogonalization, T_1 strongly localizes on the BODIPY moiety, whereas T_2 becomes a purely CT excitation, like the lowest excited singlet. As a consequence, at the perpendicular arrangement S_1/T_2 are nearly degenerate and present a small SOC, in accordance with El Sayed's rule. Simultaneously, the S_1/T_1 energy gap (SOC) decreases (increases) considerably. We note that despite the reduction of the singlet-triplet gap, it remains rather large (Figure 9a). On the other hand, it is well-known that TDDFT functionals tend to underestimate and overestimate the energy of T_1 and S_1, respectively.[78] Therefore, these results make us to conclude that ISC in **2b** (and **2c**) is triggered by the excited state relaxation via the BODIPY-enamine torsion, and takes place through the SOCT-ISC mechanism between the CT excited singlet and low-lying triplets, in particular the BODIPY-localized T_1 state, but also the second excited triplet T_2.

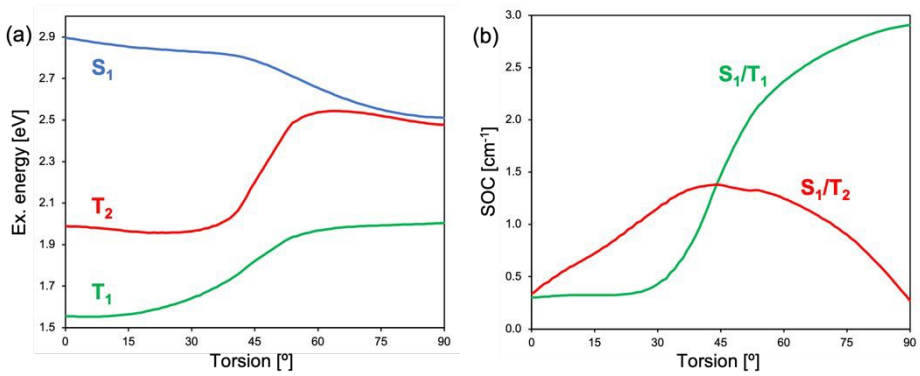

Figure 9. (a) Excitation energy (in eV with respect to the ground state at the planar geometry) of the lowest excited singlet (S_1) and triplet (T_1 and T_2) states and (b) singlet/triplet SOCs computed in ACN of **2c** along the molecular torsion between BODIPY and enamine moieties.

To further characterize the energy of the lowest triplet state (T_1), luminescence measurements are recorded at 78 K for **2c** (Figure S7). The band placed at 655 nm was assigned to phosphorescence emission, with average lifetimes in the ms range. The energy of this low-lying triplet state (182.8 kJ/mol) is higher than the energy gap between the triplet ground state of O_2 ($^3\Sigma_g$) and the first singlet excited state ($^1\Delta_g$) of O_2 (94.2 kJ/mol), fulfilling the necessary condition to generate singlet oxygen by type-II energy transfer mechanism (Figure 1). Being **2c** the best compound of the series in terms of singlet oxygen quantum production and fluorescence efficiency, a more π-conjugated *meso*-enamine BODIPY, Figure 2, **2d**, was formulated. By attaching ethynyl phenyl groups at 2 and 6 positions a notable shift is reached in both absorption and emission bands (Figure S8), resulting in an even better balance between fluorescence and singlet oxygen quantum yields (Tables 1 and S1), and showing a relatively long lived triplet state near to 100 μs (Figure S4, Table S4). Hence, **2d** could be considered as a purely organic agent

with a suitable balance between fluorescence and singlet oxygen capacities with potential use in theragnostic applications.

3.4. *In vitro* tests

Compound **2d** was selected as the most suitable enamine-BODIPY to perform assays in HeLa cells. Subcellular localization experiments confirm that **2d** can be internalized inside cells, allowing a sharp fluorescence imaging following a typical lipid droplets pattern, indicative of a selective accumulation (Figure 10A). Taking into account the broad fluorescence emission spectrum of compound **2d**, it was not possible to carry out colocalization experiments with commercial organelle-targeted fluorescent probes, since emission of probes and compound **2d** would overlap. However, Supplementary Figure S9, shows that the subcellular distribution pattern of compound **2d** is absolutely similar to that of lipid droplets, and besides, quite different from mitochondria or lysosomes in HeLa cells. Interestingly, the fluorescence image obtained with **2d** is much sharper and brighter than compound **1**, besides its lower fluorescence efficiency (Table 1).

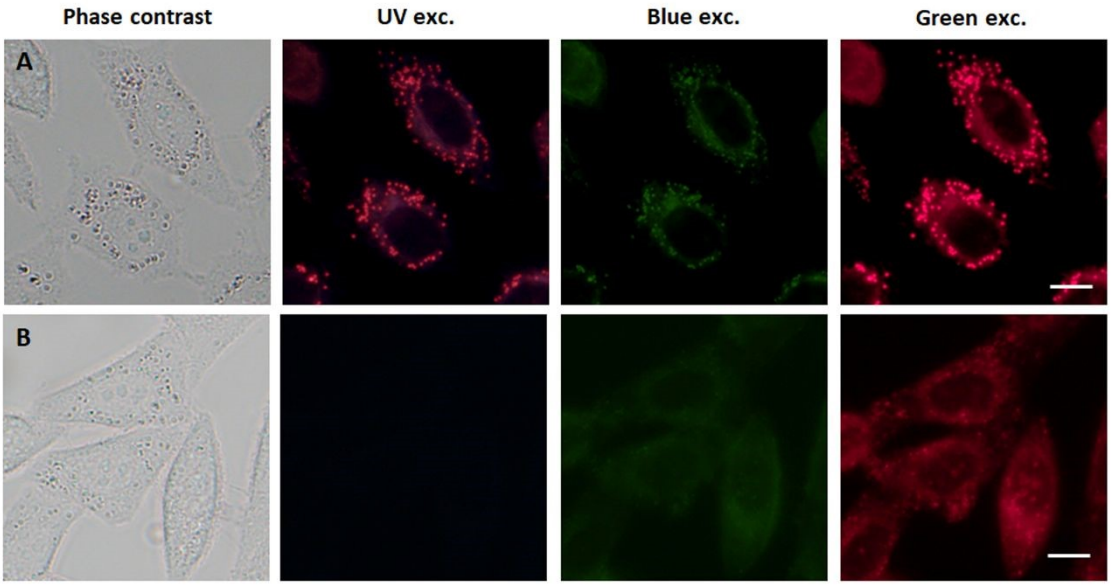

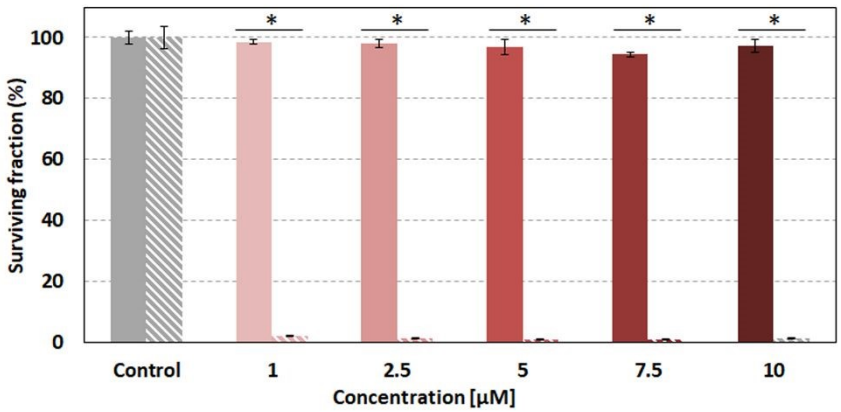

Figure 10. Top); Fluorescence microscopy images of HeLa cells incubated with **2d** (A) and **1** (B). Bottom) MTT assay results of **2d** under dark conditions (striped bars) and green irradiation (plain bars; 10 J/cm^2). Scale bar: 10 μm. Statistical significance for surviving-fraction was obtained by using one-way ANOVA. Statistically significant differences are labelled as * ($p < 0.001$).

Given the better performance of **2d** in cellular internalization, we selected this compound for further experiments in order to assess its phototoxicity. After 24 h incubation with **2d** and 10 J/cm^2 irradiation with 518 nm light, HeLa cells viability was evaluated by MTT assay. Results shown below (Figure 10) demonstrate that **2d** induces a high phototoxicity after green irradiation at low light doses (10 J/cm^2) even at the lowest **2d** concentration assayed (98% of cell death at 1 μM). Null or very low dark toxicity was detected in our experimental conditions.

4. Conclusions

The study evidences that *meso*-enamine-BODIPYs are a new family of structurally simple and easily accessible BODIPYs with the capability to act as halogen-free $^1O_2$ photosensitizers for PDT or even for theragnosis based on PDT and fluorescence. The attachment of an enamine group (electron-donor) at the *meso* position activates a charge transfer state, key to populate the triplet state via SOCT-ISC. This mechanism is triggered by the excited state relaxation via the BODIPY-enamine torsion (towards orthoganization), taking place between the CT excited singlet and low-lying triplets, in particular the BODIPY-localized T_1 state, but also the second excited triplet T_2.

Theoretical simulations and experimental characterization of the excited state relaxation by femto-transient absorption, demonstrated that the formation and energetic stabilization of a CT state induces a faster deactivation kinetics, promoted by the polarity of the solvent and/or alkylation of the BODIPY core (mainly at 1- and 7-position), accelerate non-radiative decay rates hindering singlet oxygen generation and fluorescence ability. In fact, the CT state must be formed with a sufficient lifetime (timescale set at ≥ 1.8ns) to allow the population of triplet states.

The rational design of a *meso*-enamine BODIPY without alkylation at C1 and C7, but with extended conjugation at C2 and C6, has demonstrated its viability as a biomarker of lipid droplets and photosensitizer agent in HeLa cells being very photoefficient under low green light doses (10 J/cm^2) and low concentration (≤ 1μM) and no cytotoxic under dark conditions.

Further studies to explore the possibility of development red-absorbing photosensitizers based on the present strategy (enamine group at *meso* position of the BODIPY core) by the introduction of larger extended π-conjugated moieties at C2 and C6 and/or at C3 and C5 positions would be interesting to research.

Data availability

All of the additional information and experimental data is in the ESI.†

Author contributions

A.P.-C., A.R.A. and M.J.O. synthetized and chemically characterized all compounds. R.P.-M. and V.M.-M. measured photophysical properties. A.L. and R.M. carried out the femtosecond

measurements. A.D.A. and D.C. performed theoretical simulations. A.T. and A.V. conducted *in vitro* assays. R.M, D.C. and V.M.-M wrote the manuscript. V.M.-M. revised and edit the final manuscript. V.M.-M. conceived and supervised the study. All authors have read and agreed to the published version of the manuscript.

Conflicts of interest

There are no conflicts to declare.

Acknowledgments

This work was funded by MCIN/AEI/10.13039/501100011033 (projects No. PID2020-114347RB-C32, PID2020-114755GB-C31, PID2019-109555GB-I00 and RED2018-102815-T) and from Gobierno Vasco (project No. IT1639-22 and PIBA19-0004). R.P.-M. and A.D.A. thanks UPV/EHU, MIU and NGEU for their respective postdoctoral (MARSA21/71) and predoctoral (PRE2020-092036) fellowships. We also thank the SGIker Laser Facility of the UPV/EHU for the technical support.

References

1 S. S. Kelkar and T. M. Reineke, *Bioconjugate Chemistry*, 2011, **22**, 1879–1903.
2 A. Yordanova, E. Eppard, S. Kürpig, R. A. Bundschuh, S. Schönberger, M. Gonzalez-Carmona, G. Feldmann, H. Ahmadzadehfar and M. Essler, *OncoTargets and Therapy*, 2017, **10**, 4821–4828.
3 S. Navalkissoor, G. Gnanasegaran and R. Baum, *The British journal of radiology*, 2018, **91**, 20189004–20189012.
4 D. van Straten, V. Mashayekhi, H. de Bruijn, S. Oliveira and D. Robinson, *Cancers*, 2017, **9**, 19–73.
5 E. K. Lim, T. Kim, S. Paik, S. Haam, Y. M. Huh and K. Lee, *Chemical Reviews*, 2015, **115**, 327–394.
6 R. Kumar, W. S. Shin, K. Sunwoo, W. Y. Kim, S. Koo, S. Bhuniya and J. S. Kim, *Chemical Society Reviews*, 2015, **44**, 6670–6683.
7 W. Hu, H. Ma, B. Hou, H. Zhao, Y. Ji, R. Jiang, X. Hu, X. Lu, L. Zhang, Y. Tang, Q. Fan and W. Huang, *ACS Applied Materials and Interfaces*, 2016, **8**, 12039–12047.
8 W. Hu, X. Miao, H. Tao, A. Baev, C. Ren, Q. Fan, T. He, W. Huang and P. N. Prasad, *ACS Nano*, 2019, **13**, 12006–12014.
9 B. Yang, Y. Chen and J. Shi, *Advanced Materials*, 2019, **31**, 1–33.
10 X. Li, S. Kolemen, J. Yoon and E. U. Akkaya, *Advanced Functional Materials*, 2017, **27**, 1–11.
11 B. del Rosal, B. Jia and D. Jaque, *Advanced Functional Materials*, 2018, **28**, 1–25.
12 C. N. Ko, G. Li, C. H. Leung and D. L. Ma, *Coordination Chemistry Reviews*, 2019, **381**, 79–103.
13 M. DeRosa, *Coordination Chemistry Reviews*, 2002, **233–234**, 351–371.
14 C. Hopper, *Lancet Oncology*, 2000, **1**, 212–219.
15 K. Moghissi, K. Dixon and S. Gibbins, *The Surgery Journal*, 2015, **01**, e1–e15.
16 H. T. Bui, D. K. Mai, B. Kim, K.-H. Choi, B. J. Park, H.-J. Kim and S. Cho, *The Journal of Physical Chemistry B*, 2019, **123**, 5601–5607.
17 D. E. J. G. J. Dolmans, D. Fukumura and R. K. Jain, *Nature Reviews Cancer*,

2003, **3**, 380–387.
18 B. Kim, B. Sui, X. Yue, S. Tang, M. G. Tichy and K. D. Belfield, *European Journal of Organic Chemistry*, 2017, **2017**, 25–28.
19 C. S. Kue, S. Y. Ng, S. H. Voon, A. Kamkaew, L. Y. Chung, L. V. Kiew and H. B. Lee, *Photochemical & Photobiological Sciences*, 2018, **17**, 1691–1708.
20 A. Kamkaew, S. H. Lim, H. B. Lee, L. V. Kiew, L. Y. Chung and K. Burgess, *Chemical Society reviews*, 2013, **42**, 77–88.
21 G. Durán-Sampedro, N. Epelde-Elezcano, V. Martínez-Martínez, I. Esnal, J. Bañuelos, I. García-Moreno, A. R. Agarrabeitia, S. de la Moya, A. Tabero, A. Lazaro-Carrillo, A. Villanueva, M. J. Ortiz and I. López-Arbeloa, *Dyes and Pigments*, 2017, **142**, 77–87.
22 S. Zhen, S. Wang, S. Li, W. Luo, M. Gao, L. G. Ng, C. C. Goh, A. Qin, Z. Zhao, B. Liu and B. Z. Tang, *Advanced Functional Materials*, 2018, **28**, 1–15.
23 P. R. Ogilby, *Chemical Society Reviews*, 2010, **39**, 3181–3209.
24 N. Boens, B. Verbelen, M. J. Ortiz, L. Jiao and W. Dehaen, *Coordination Chemistry Reviews*, 2019, **399**, 213024–213109.
25 A. Treibs and F.-H. Kreuzer, *Justus Liebigs Annalen der Chemie*, 1968, **718**, 208–223.
26 F. López Arbeloa, J. Bañuelos, V. Martínez, T. Arbeloa and I. López Arbeloa, *International Reviews in Physical Chemistry*, 2005, **24**, 339–374.
27 X. F. Zhang and J. Zhu, *Journal of Luminescence*, 2019, **205**, 148–157.
28 R. Prieto-Montero, A. Prieto-Castañeda, R. Sola-Llano, A. R. Agarrabeitia, D. García-Fresnadillo, I. López-Arbeloa, A. Villanueva, M. J. Ortiz, S. Moya and V. Martínez-Martínez, *Photochemistry and Photobiology*, 2020, **96**, 458–477.
29 R. Padrutt, V. Babu, S. Klingler, M. Kalt, F. Schumer, M. I. Anania, L. Schneider and B. Spingler, *ChemMedChem*, 2020, 694–701.
30 J. Zhao, K. Xu, W. Yang, Z. Wang and F. Zhong, *Chemical Society Reviews*, 2015, **44**, 8904–8939.
31 T. Yogo, Y. Urano, Y. Ishitsuka, F. Maniwa and T. Nagano, *Journal of the American Chemical Society*, 2005, **127**, 12162–12163.
32 I. S. Turan, G. Gunaydin, S. Ayan and E. U. Akkaya, *Nature Communications*, 2018, **9**, 1–8.
33 W. Wu, Y. Geng, W. Fan, Z. Li, L. Zhan, X. Wu, J. Zheng, J. Zhao and M. Wu, *RSC Advances*, 2014, **4**, 51349–51352.
34 S. G. Awuah and Y. You, *RSC Advances*, 2012, **2**, 11169–11183.
35 J. H. Gibbs, Z. Zhou, D. Kessel, F. R. Fronczek, S. Pakhomova and M. G. H. Vicente, *Journal of Photochemistry and Photobiology B: Biology*, 2015, **145**, 35–47.
36 R. Lincoln, A. M. Durantini, L. E. Greene, S. R. Martínez, R. Knox, M. C. Becerra and G. Cosa, *Photochemical and Photobiological Sciences*, 2017, **16**, 178–184.
37 J. Zou, Z. Yin, K. Ding, Q. Tang, J. Li, W. Si, J. Shao, Q. Zhang, W. Huang and X. Dong, *ACS Applied Materials and Interfaces*, 2017, **9**, 32475–32481.
38 A. J. Sánchez-Arroyo, E. Palao, A. R. Agarrabeitia, M. J. Ortiz and D. García-Fresnadillo, *Phys. Chem. Chem. Phys.*, 2017, **19**, 69–72.
39 A. Turksoy, D. Yildiz and E. U. Akkaya, *Coordination Chemistry Reviews*, 2019, **379**, 47–64.
40 V. N. Nguyen, Y. Yan, J. Zhao and J. Yoon, *Accounts of Chemical Research*, 2021, **54**, 207–220.
41 Y. Dong, A. Elmali, J. Zhao, B. Dick and A. Karatay, *ChemPhysChem*, 2020, **21**,

1388–1401.
42 J. W. Verhoeven, *Journal of Photochemistry and Photobiology C: Photochemistry Reviews*, 2006, **7**, 40–60.
43 Z. J. Jakubek, M. Chen, M. Couillard, T. Leng, L. Liu, S. Zou, U. Baxa, J. D. Clogston, W. Y. Hamad and L. J. Johnston, *Journal of Nanoparticle Research*, 2018, **20**, 1–10.
44 Y. Zhao, R. Duan, J. Zhao and C. Li, *Chemical Communications*, 2018, **54**, 12329–12332.
45 X. F. Zhang and N. Feng, *Chemistry - An Asian Journal*, 2017, **12**, 2447–2456.
46 Z. Wang, M. Ivanov, Y. Gao, L. Bussotti, P. Foggi, H. Zhang, N. Russo, B. Dick, J. Zhao, M. Di Donato, G. Mazzone, L. Luo and M. Fedin, *Chemistry – A European Journal*, 2020, **26**, 1091–1102.
47 J. Jiménez, R. Prieto-Montero, B. L. Maroto, F. Moreno, M. J. Ortiz, A. Oliden-Sánchez, I. López-Arbeloa, V. Martínez-Martínez and S. de la Moya, *Chemistry - A European Journal*, 2020, **26**, 601–605.
48 W. Hu, Y. Lin, X. F. Zhang, M. Feng, S. Zhao and J. Zhang, *Dyes and Pigments*, 2019, **164**, 139–147.
49 T. C. Pham, S. Heo, V. N. Nguyen, M. W. Lee, J. Yoon and S. Lee, *ACS Applied Materials and Interfaces*, 2021, **13**, 13949–13957.
50 V. N. Nguyen, S. J. Park, S. Qi, J. Ha, S. Heo, Y. Yim, G. Baek, C. S. Lim, D. J. Lee, H. M. Kim and J. Yoon, *Chemical Communications*, 2020, **56**, 11489–11492.
51 L. A. Ortiz-Rodríguez and C. E. Crespo-Hernández, *Chemical Science*, 2020, **11**, 11113–11123.
52 V. N. Nguyen, S. Heo, C. W. Koh, J. Ha, G. Kim, S. Park and J. Yoon, *ACS Sensors*, 2021, **6**, 3462–3467.
53 W. Hu, X.-F. Zhang and M. Liu, *The Journal of Physical Chemistry C*, 2021, **125**, 5233–5242.
54 X. Wang, Y. Song, G. Pan, W. Han, B. Wang, L. Cui, H. Ma, Z. An, Z. Xie, B. Xu and W. Tian, *Chemical Science*, 2020, **11**, 10921–10927.
55 E. A. Weiss, M. A. Ratner and M. R. Wasielewski, *Journal of Physical Chemistry A*, 2003, **107**, 3639–3647.
56 D. Liu, A. M. El-Zohry, M. Taddei, C. Matt, L. Bussotti, Z. Wang, J. Zhao, O. F. Mohammed, M. Di Donato and S. Weber, *Angewandte Chemie - International Edition*, 2020, **59**, 11591–11599.
57 M. A. Filatov, *Organic and Biomolecular Chemistry*, 2019, **18**, 10–27.
58 D. J. Gibbons, A. Farawar, P. Mazzella, S. Leroy-Lhez and R. M. Williams, *Photochemical and Photobiological Sciences*, 2020, **19**, 136–158.
59 Y. Dong, A. A. Sukhanov, J. Zhao, A. Elmali, X. Li, B. Dick, A. Karatay and V. K. Voronkova, *Journal of Physical Chemistry C*, 2019, **123**, 22793–22811.
60 X. F. Zhang and X. Yang, *Journal of Physical Chemistry B*, 2013, **117**, 9050–9055.
61 E. Bassan, A. Gualandi, P. G. Cozzi and P. Ceroni, *Chemical Science*, 2021, **12**, 6607–6628.
62 L. A. Ortiz-Rodríguez, S. J. Hoehn, A. Loredo, L. Wang, H. Xiao and C. E. Crespo-Hernández, *Journal of the American Chemical Society*, 2021, **143**, 2676–2681.
63 A. A. Buglak, A. Charisiadis, A. Sheehan, C. J. Kingsbury, M. O. Senge and M. A. Filatov, *Chemistry – A European Journal*, 2021, **27**, 9934–9947.
64 S. Rihn, P. Retailleau, N. Bugsaliewicz, A. De Nicola and R. Ziessel,

Tetrahedron Letters, 2009, **50**, 7008–7013.
65 M. A. Filatov, S. Karuthedath, P. M. Polestshuk, S. Callaghan, K. J. Flanagan, T. Wiesner, F. Laquai and M. O. Senge, *ChemPhotoChem*, 2018, **2**, 606–615.
66 Y. Dong, B. Dick and J. Zhao, *Organic Letters*, 2020, **22**, 5535–5539.
67 J. Zhao, K. Chen, Y. Hou, Y. Che, L. Liu and D. Jia, *Organic and Biomolecular Chemistry*, 2018, **16**, 3692–3701.
68 J. B. Prieto, F. L. Arbeloa, V. M. Martínez, T. A. López and I. L. Arbeloa, *Journal of Physical Chemistry A*, 2004, **108**, 5503–5508.
69 M. A. Filatov, S. Karuthedath, P. M. Polestshuk, H. Savoie, K. J. Flanagan, C. Sy, E. Sitte, M. Telitchko, F. Laquai, R. W. Boyle and M. O. Senge, *Journal of the American Chemical Society*, 2017, **139**, 6282–6285.
70 E. Palao-Utiel, L. Montalvillo-Jiménez, I. Esnal, R. Prieto-Montero, A. R. Agarrabeitia, I. García-Moreno, J. Bañuelos, I. López-Arbeloa, S. de la Moya and M. J. Ortiz, *Dyes and Pigments*, 2017, **141**, 286–298.
71 I. Esnal, I. Valois-Escamilla, C. F. A. Gómez-Durán, A. Urías-Benavides, M. L. Betancourt-Mendiola, I. López-Arbeloa, J. Bañuelos, I. García-Moreno, A. Costela and E. Peña-Cabrera, *ChemPhysChem*, 2013, **14**, 4134–4142.
72 V. P. Yakubovskyi, M. P. Shandura and Y. P. Kovtun, *Dyes and Pigments*, 2010, **87**, 17–21.
73 N. Epelde-Elezcano, E. Palao, H. Manzano, A. Prieto-Castañeda, A. R. Agarrabeitia, A. Tabero, A. Villanueva, S. de la Moya, Í. López-Arbeloa, V. Martínez-Martínez and M. J. Ortiz, *Chemistry - A European Journal*, 2017, **23**, 4837–4848.
74 Y. Liu, J. Zhao, A. Iagatti, L. Bussotti, P. Foggi, E. Castellucci, M. Di Donato and K. L. Han, *Journal of Physical Chemistry C*, 2018, **122**, 2502–2511.
75 R. Montero, V. Martínez-Martínez, A. Longarte, N. Epelde-Elezcano, I. Lamas and I. L. Arbeloa, *Journal of Physical Chemistry Letters*, 2021, **12**, 7439–7441.
76 Y. Lee, R. M. Malamakal, D. M. Chenoweth and J. M. Anna, *Journal of Physical Chemistry Letters*, 2020, **11**, 877–884.
77 Q. Zhou, M. Zhou, Y. Wei, X. Zhou, S. Liu, S. Zhang and B. Zhang, *Physical Chemistry Chemical Physics*, 2017, **19**, 1516–1525.
78 V. Postils, F. Ruipérez and D. Casanova, *Journal of Chemical Theory and Computation*, 2021, **17**, 5825–5838.